# An End-to-End Signal Processing Chain for Low Earth Orbit Inverse Synthetic Aperture Radar Space Object Imaging

## Tim Jennings-Bramly, Jonathan Maxey
*Defence Science Technology Laboratory (Dstl)*

## ABSTRACT

The UK Ministry of Defence (MOD) is carrying out research into the design, demonstration and operational use of ground-based Inverse Synthetic Aperture Radar (ISAR) for characterising Resident Space Objects (RSOs). In support of this, Defence Science and Technology Laboratory (Dstl) has begun the development of ISAR signal processing and simulation models for use in assessing system requirements in relation to UK civilian and military Space Domain Awareness (SDA) requirements. The modelling capability developed as part of this work, along with illustrative examples, is presented in this paper.

While primarily limited by radar hardware, the quality of an ISAR image is inherently dependent on the signal processing chain. In particular, the choice of Translational Motion Compensation (TMC) and Rotational Motion Compensation (RMC) algorithms can impact the quality of an ISAR image significantly. This paper provides a brief overview of TMC and RMC algorithms; it will then follow with a more detailed assessment of the suitability of various RMC algorithms for Space Object Imaging (SOI). A simulation of representative orbital scenarios has been created to test the signal processing methods, the results of which have then been used to formulate a complete end-to-end signal processing chain for ISAR SOI. We describe how the proposed signal processing chain can be used to characterise space objects, both by using the resolved image and also by using derived object motion parameters output by the methods themselves. We also simulate a Rendezvous and Proximity Operation (RPO) scenario and evaluate the performance of the proposed signal processing chain for producing resolved images of RSOs undergoing close-proximity manoeuvres.

## 1. INTRODUCTION

Traditional SDA-capable sensors such as the Upgraded Early Warning Radar at RAF Fylingdales are typically capable of detecting Resident Space Objects (RSOs) at long range within large regions of sky enabling the sensor to gather data on many RSOs simultaneously. The data gathered by such a system is usually numeric (e.g. position, velocity and reflectivity) and is primarily used for updating the state estimate of an orbiting RSO. Data of this kind can also be used to provide limited characterisation capability. For example, reflectivity time-variations can be used to infer RSO attitude, and differences between observations and expectations can be used to infer changes of state. However, as the RSO population continues to grow [1] and the number of conjunctions increases, there is an increasing demand in both military and civil circles for systems that will provide an improved characterisation capability. In particular, systems capable of providing damage assessment and monitoring of close-proximity operations such as active debris removal are in especially high demand. Improved characterisation could also enhance traditional SDA sensors by informing the prioritisation of RSOs during state estimate update procedures.

One proposed solution to improve characterisation capability is to develop an SDA system capable of producing resolved imagery of a small number of high-priority RSOs. With sufficient resolution, such imagery could be used to perform RSO identification and/or identify individual features such as solar panels, antennas and payloads. Further characterisation performance can be extracted if a number of resolved images are collected over a given period of time. In particular, a time-series of images could be used to infer operational status by evaluating changes to the RSO's pattern of life.

Low Earth Orbit (LEO) Space Object Imaging (SOI) is often achieved with optical or radar sensors, however, it can be difficult to produce resolved imagery of objects using ground-based optical sensors due to atmospheric and weather effects. Furthermore, possible imaging windows are typically limited to night-time hours and to periods when the spacecraft is illuminated by the Sun. In contrast, Inverse Synthetic Aperture Radar (ISAR) can be used to image objects at all times of the day. High power amplification and large antennas can be used to image RSOs at orbital ranges and wideband radar technology can be used to produce centimeter-level resolutions.

**Paper layout:**
This paper will begin with a brief overview of ISAR image formation theory before discussing the performance and selection of motion compensation algorithms in the following section. The chosen algorithms will then be tested against representative 3D orbital scenarios as part of an end-to-end ISAR signal processing chain. Finally, the signal processing chain will be applied to a simulated RPO scenario.

## 2. ISAR IMAGE FORMATION THEORY

### 2.1 Scatterer theory

When an Electro-Magnetic (EM) wave is incident on a target, the reflected wave is dependent on local reflections, diffractions, surface waves and ducting caused by the target's geometric and material properties. The sum of these interactions cause different parts of the target to contribute more/less to the reflected wave. When an image of the target is resolved, parts of the target that contribute more to the reflected wave appear brighter. The bright areas on the target vary depending on its aspect angle and the incident frequency of the EM wave, but are typically located in corner-reflectors and on planar surfaces oriented normal to the radar.
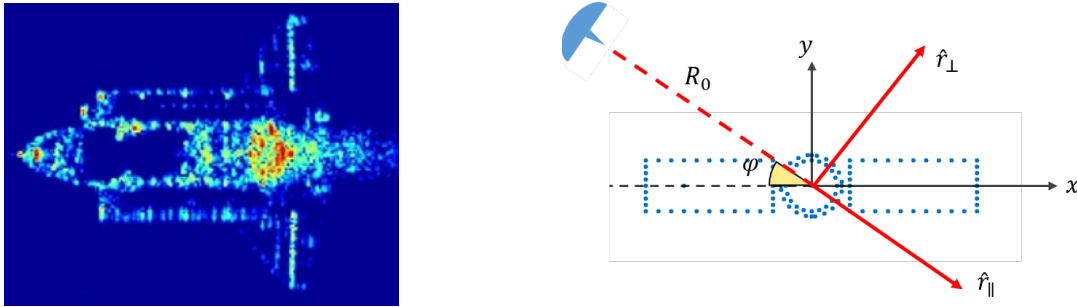


Fig. 1 ISAR image processed by DERA staff using data provided to the UK MOD by the US (left). Example point scatterer target depicting a cylindrical satellite with solar panel "wings" in the ISAR reference frame (right).

These bright areas on the target can be approximated as perfectly reflecting point scatterers each with a Radar Cross Section (RCS) scaled by the brightness of the area [2]. In this paper, we use highly approximated point scatterer models to simulate the reflected signal from a target whereby the RCS of the scatterers are equal and unchanging with aspect angle. By calculating the received signal from each of the point scatterers and summing them together, we can approximate the received signal from a target. The position vector of the $n^{\text{th}}$ scatterer relative to the radar, $\vec{R}_n$ at any given aspect angle, $\varphi$ is given by:

$$\vec{R}_n = [R_0 + x_n \cos(\varphi) - y_n \sin(\varphi)]\hat{r}_\parallel + [x_n \sin(\varphi) + y_n \cos(\varphi)]\hat{r}_\perp + z_n \hat{\varphi}$$

Where $R_0$ is the distance between the radar and the target's centre of mass, $(x_n, y_n)$ is the position of the $n^{\text{th}}$ scatterer in the body-fixed frame relative to the target's centre of mass, and $\hat{\varphi} = \hat{r}_\parallel \times \hat{r}_\perp$. The target is often far from the radar resulting in the $\hat{r}_\parallel$ term being much larger than the $\hat{r}_\perp$ and $\hat{\varphi}$ terms. In this case, we can approximate the range to the scatterer as:

$$R_n \approx R_0 + x_n \cos(\varphi) - y_n \sin(\varphi) \tag{1}$$

It is also common for the change in target aspect angle during the imaging period to be small. In this case, we can use the first term of the Taylor series expansion for $\cos(\varphi)$ and $\sin(\varphi)$ to further approximate the range to the scatterer using the following equation (this is a standard approximation in ISAR literature and is justified for the high carrier frequencies typically used by ISAR systems – this will be demonstrated in the following sections):

$$R_n \approx R_0 + x_n - y_n \varphi \tag{2}$$

### 2.2 Range profile formation

An ISAR system will typically transmit a frequency modulated pulse in order to improve its range-resolution and discriminate between closely separated scattering centres. Linear Frequency Modulation (LFM) is commonly used. The transmitted LFM signal is given by the following equation:

$$s_{Tx}(t) = Ae^{-j2\pi\left[f_0 t + \frac{B}{2\tau}t^2\right]} \qquad (0 \leq t \leq \tau)$$

Where $A$ is the amplitude of the transmitted waveform, $f_0$ is the transmitted frequency at the start of the chirp, $B$ is the bandwidth of the transmitted signal, $\tau$ is the pulse width, and $t$ is time. When this LFM signal is incident on a target composed of $N$ perfectly reflecting scatterers, the reflected signal is given by the following equation:

$$s_{Rx}(t) = \sum_{n=1}^{N} A_n e^{-j2\pi\left[f_0\beta_n(t-t_n) + \frac{B}{2\tau}\beta_n^2(t-t_n)^2\right]} \qquad (t_n \leq t \leq t_n + \tau)$$

Where $t_n$ is the signal's delay, $\beta_n$ is the time dilation factor and $A_n$ is the amplitude of the wave reflected from the $n^{\text{th}}$ scatterer. Note that delay is related to range by $t = \frac{2R}{c}$ and the time dilation factor is related to velocity relative to the radar by $\beta = 1 - \frac{2v}{c}$. If the position and velocity of the target is approximately known (e.g. by using an accompanying tracking radar system), the received signal can be de-chirped by mixing it with a stretch-processing signal defined as follows:

$$s_{stretch}(t) = e^{j2\pi\left[f_0\beta_g(t-t_g) + \frac{B}{2\tau}\beta_g^2(t-t_g)^2\right]}$$

Where $t_g$ is the estimated delay and $\beta_g$ is the estimated time dilation factor of the target's centre of mass relative to the radar; these values are typically estimated using measurements from an accompanying tracking system. The stretch signal is generated over a larger time window than the transmitted signal to ensure that the stretch signal mixes with the entire duration of the reflected signal. Mixing these signals via multiplication results in a new signal given by, $s(t) = s_{Rx}(t) \cdot s_{stretch}(t)$. Defining the time axis relative to the estimated delay, $\Delta = t - t_g$ gives:

$$s(\Delta) = \sum_{n=1}^{N} e^{j2\pi\left[f_0\beta_n + \frac{B}{2\tau}\beta_n^2(t_n+t_g)\right](t_n-t_g)} \cdot e^{j2\pi\left[f_0(\beta_g-\beta_n) + \frac{B}{\tau}\beta_n^2(t_n-t_g)\right]\Delta} \cdot e^{j2\pi\frac{B}{2\tau}(\beta_g^2-\beta_n^2)\Delta^2}$$

The resulting signal exhibits beat frequencies approximately proportional to the difference in true and estimated signal delays. A Fourier transform of the above expression can be used to pick out these beat frequencies:

$$|S(f)| \approx \tau \cdot \left|\text{sinc}\left\{\pi\left[\frac{B}{\tau}(t_n - t_g) - f\right]\tau\right\}\right|$$

Since there will be some error in the estimated delay to the target's centre of mass, we can say that $t_g = \frac{2(R_0+\Delta R)}{c}$ so that $t_n - t_g = \frac{2(x_n - \Delta R)}{c}$ where $\Delta R$ is an error term. Substituting this into the above expression and scaling the beat-frequency axis using $f = \frac{2B}{c\tau}x$, we can show that the distribution of beat frequencies describes a range profile of the target with a resolution defined by the -3dB width of the sinc function's mainlobe, $\Delta x = \frac{c}{2B}$:

$$|S(x)| \approx \tau \cdot \left|\text{sinc}\left\{\pi\frac{2B}{c}[(x_n - \Delta R) - x]\right\}\right|$$

## 2.3 Sample storage

The cross-range resolution of a traditional radar is proportional to the size of its beam-width, and therefore its aperture. In order to obtain fine cross-range resolutions, ISAR systems can make use of the target's relative rotation to form large synthetic apertures. A synthetic aperture is formed by transmitting a number of pulses over a period called the Coherent Processing Interval (CPI). These pulses reflect off the target and are de-chirped as described in the previous section before being sampled by the radar at a fixed rate, $f_{samp}$. In particular, the radar measures the de-chirped signal's amplitude and phase at each sample time. The amplitude and phase samples are stored as complex numbers in a matrix where each row corresponds to the pulse transmission time or "slow-time" ($\eta$) and each column corresponds to the sample time or "fast-time" ($\Delta$). This matrix can be plotted as a heatmap to visualise the collection of sampled pulses (see Fig. 2, left).
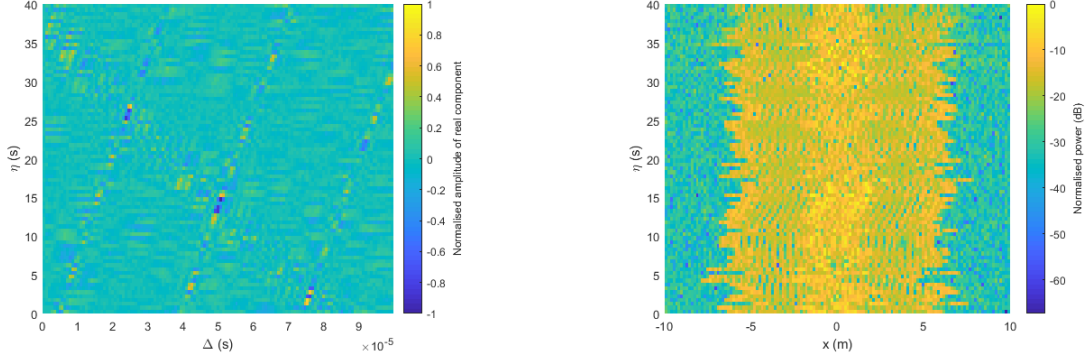
Fig. 2 Matrix of de-chirped signal samples (left). Associated range profiles after Fourier transforming each row (right).

As described in section 2.2, Fourier transforming along each row (fast-time axis) of this matrix will result in a series of range profiles associated with a pulse transmission time. Again, we can plot the result as a heat map. Since the estimated position of the target's centre of mass is never known precisely, the error term $\Delta R$ is usually non-zero. This results in a set of range profiles that are poorly aligned with each other (see Fig. 2, right).

## 2.4 Translational Motion Compensation

Translational Motion Compensation (TMC) algorithms can be used to estimate $\Delta R$ for each range profile – we will briefly discuss these algorithms in section 3. These $\Delta R$ estimates can then be used to further estimate the delay $t_0$ and time dilation factor $\beta_0$ of the target's centre of mass for each range profile. With this information, we can centre each range profile by first multiplying each de-chirped signal with a corrective function, $m(\Delta)$ [3]:

$$m(\Delta) = e^{-j2\pi\left[f_0+\frac{B}{\tau}\Delta\right](t_0-t_g)} \cdot e^{-j2\pi f_0\Delta(\beta_0-\beta_g)}$$

$$s_{corr}(\Delta) = s(\Delta) \cdot m(\Delta) \approx \sum_{n=1}^{N} e^{j2\pi\left[f_0+\frac{B}{\tau}\Delta\right](t_n-t_0)}$$

The Fourier transform of the resulting function, $s_{corr}(\Delta)$ describes a range profile of the target with its centre of mass located at $x = 0$. If we scale the beat-frequency axis using $f = \frac{2B}{c\tau}x$ again, we obtain equation 3:

$$S_{corr}(x) \approx \sum_{n=1}^{N} B \cdot e^{j4\pi\frac{f_c}{c}[(R_n-R_0)-x]} \cdot \text{sinc}\left\{\pi\frac{2B}{c}[(R_n-R_0)-x]\right\} \tag{3}$$

The target's rotation rate is often approximately constant during the imaging period, $\varphi \approx \dot{\varphi}\eta$. Substituting this approximation into equations 2 and 3, we obtain equation 4:

$$S_{corr}(x,\eta) \approx \sum_{n=1}^{N} B \cdot e^{j4\pi\frac{f_c}{c}[(x_n-y_n\dot{\varphi}\eta)-x]} \cdot \text{sinc}\left\{\pi\frac{2B}{c}(x_n-x)\right\} \tag{4}$$
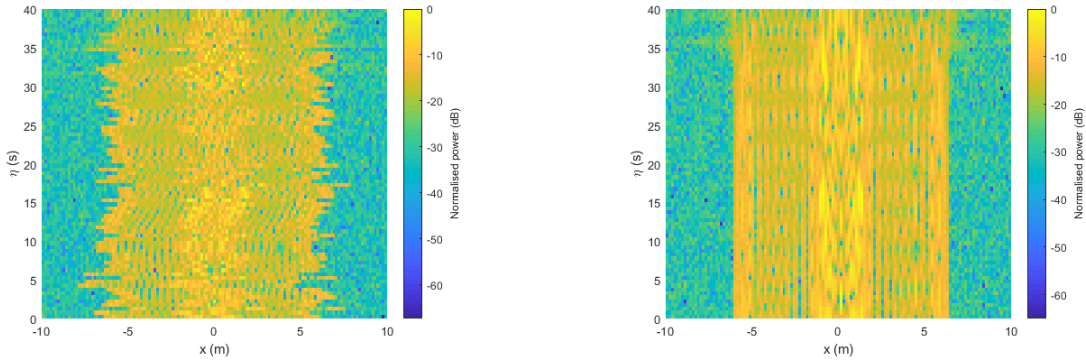


Fig. 3 Range profiles before (left) and after (right) alignment.

## 2.5    Image formation

Once aligned, the range profiles now appear to originate from a target rotating about its centre of mass at a fixed distance from the radar. If the target is rigid, the scatterers will all be rotating with the same angular velocity. This means that the velocity of each scatterer relative to the radar will vary linearly with respect to its cross-range position, $v_n = y_n\dot\varphi$. The velocities result in subtle red/blue Doppler shifts that can be measured by applying an inverse Fourier transform along each column (slow-time axis) of the aligned range-profiles. This results in a range-Doppler image described by:

$$f_{D_n} = \frac{2y_n\dot\varphi}{c}f_c$$

$$|I_{rD}(x, f_D)| \approx \sum_{n=1}^{N} B \cdot CPI \cdot \text{sinc}\left[\pi\frac{2B}{c}(x_n - x)\right] \cdot \text{sinc}\left[\pi(f_D - f_{D_n})CPI\right]$$

The inverse Fourier transform along the slow-time axis of a set of aligned range-profiles can therefore be used to obtain a range-Doppler image of the target with a resolution defined by the -3dB width of the sinc function, $\Delta f_D = \frac{1}{CPI}$.

## 2.6    Rotational Motion Compensation

If the CPI is too large, the small angle assumption may not be satisfied. In this case, the range-Doppler image will be rotationally blurred due to scatterers moving across range bins during the CPI (see Fig. 6). Rotational Motion Compensation (RMC) algorithms can be used to de-blur the image. They can also be used to estimate the rotational velocity of the target. Once the rotational velocity is known, the Doppler axis can be converted to a cross-range axis by scaling it according to, $f_{D_n} = \frac{2f_c\dot\varphi}{c}y_n$:

$$|I_{ISAR}(x, f_D)| \approx \sum_{n=1}^{N} B \cdot CPI \cdot \text{sinc}\left[\pi\frac{2B}{c}(x_n - x)\right] \cdot \text{sinc}\left[\pi\frac{2f_c\dot\varphi CPI}{c}(y - y_n)\right]$$

The Doppler resolution of the range-Doppler image is also scaled, resulting in a cross-range resolution defined by, $\Delta y = \frac{c}{2f_c\dot\varphi CPI}$. In this paper, we will define an ISAR image as a radar image having a scaled cross-range axis.
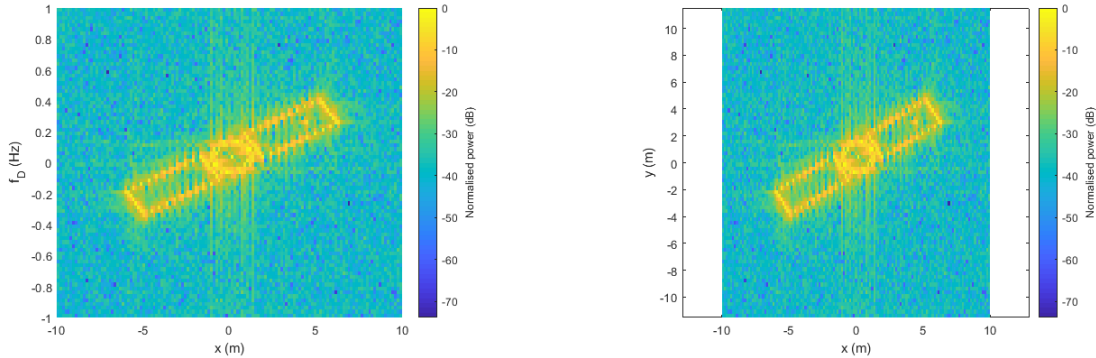


Fig. 4 (Left) Range-Doppler image formed from the aligned range profiles. (Right) ISAR image formed by scaling the Doppler axis of the range-Doppler image.

## 2.7    ISAR signal processing chain

In this section, we have briefly described the process for forming high-resolution ISAR images of a target. The steps are performed sequentially and form a complete ISAR signal processing chain once combined. For reference, Fig. 5 shows a general ISAR signal processing chain along with various places where intermediate data products can be collected. The final data product in this diagram is the "High resolution ISAR image". The next sections will look at the various types of motion compensation algorithms.
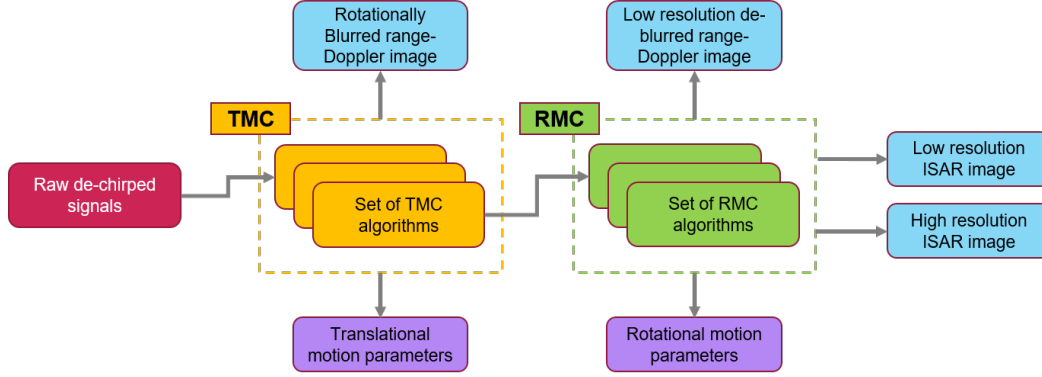
Fig. 5 An example ISAR signal processing chain structure with potential outputs shown at each stage.

### 3. TRANSLATIONAL MOTION COMPENSATION

TMC involves shifting the range profiles of a target so that the target's centre of rotation is aligned with $x = 0$. This is achieved by applying a corrective function to the stretch-processed signals as described in the previous section. There are several algorithms that can do this with varying degrees of quality. Low-performance algorithms are often used to provide initial guesses for high-performance algorithms which can result in a lengthier and more complex signal processing chain.

#### 3.1 Low-performance TMC algorithms

Common low-performance algorithms include: cross-correlation [4], range centroid [5], and range profile entropy [6]. All of these algorithms estimate the time-delay error, $t_\varepsilon(\eta) = \frac{2\Delta R(\eta)}{c}$ by optimising against a single reference range-profile. Since the target rotates between each pulse, the reference range-profile is usually chosen near the centre of the CPI to increase the degree of similarity. The accuracy of these algorithms is limited by the spacing along the range axis, but they are relatively fast to run.

#### 3.2 Medium-performance TMC algorithms

The accuracy of the corrective function can be improved by fitting a curve to the results of the low-performance TMC algorithms, $f(\eta) = t_g(\eta) + t_\varepsilon(\eta)$. This smooths the discrete results and reduces the effect of outliers on the final image. High-order polynomial fits are commonly used, however if the target motion is well known then a more accurate fitting function can be used instead.

#### 3.3 High-performance TMC algorithms

High-performance algorithms typically use image quality metrics such as image entropy ($E$) [6] and image contrast ($IC$) [7] to optimise the corrective function. Image entropy provides a measure of how disordered the image is (an unfocused image will be more disordered) and should be minimised. Image contrast provides a measure of how focused the image is and should be maximised.

$$E(I) = -\sum_{m=1}^{M} \sum_{n=1}^{N} I'[m,n] \cdot log_{10}(I'[m,n])$$

$$I'[m,n] = \frac{|I[m,n]|}{\sum_{m=1}^{M} \sum_{n=1}^{N} |I[m,n]|}$$

$$IC(I) = \frac{I_{\Delta rms}}{I_{avg}}$$

$$I_{\Delta rms} = \sqrt{\frac{\sum_{m=1}^{M} \sum_{n=1}^{N} \left(|I[m,n]| - I_{avg}\right)^2}{M \cdot N}}$$

$$I_{avg} = \frac{\sum_{m=1}^{M} \sum_{n=1}^{N} |I[m,n]|}{M \cdot N}$$

These metrics can be used to optimise the coefficients of a fitting function. If the fitting function has a small number of coefficients, this method can be relatively fast due to the small number of parameters to optimise. However, the performance of this method is highly dependent on how well the fitting function describes the translational motion of the target.

Alternatively, image quality metrics can be used to find the corrective function directly by treating each value in $t_\varepsilon(\eta)$ as a unique variable. Since there can be many pulses in a CPI, this can involve optimising over many variables and is the slowest of the discussed approaches. The speed of convergence is highly dependent on the quality of the initial guess.

### 3.4 Fine TMC algorithms

Once the range-profiles have been corrected, there may still be some residual phase noise due to slight range misalignment or other effects; however, phase accuracy over the CPI is highly important to produce a clear image. This error should therefore be reduced as much as possible. The residual phase noise acts along the slow-time axis and can be removed by multiplying the matrix of range-profiles by a phase-correction function, $e^{j\theta_\varepsilon(\eta)}$. There are several fine TMC algorithms that can be used to estimate this function, such as: Phase Gradient Autofocus (PGA) [8], dominant scatterer [9], maximum amplitude [9].

## 4. ROTATIONAL MOTION COMPENSATION

RMC involves scaling the Doppler axis and reducing the effect of rotational blurring in order to form a high-resolution ISAR image. There are two primary causes of rotational blurring:

1.  Non-planar rotations. Since the ISAR signal processing chain assumes planar rotations to form a clear image, non-planar rotations can result in noticeable overlaying. Non-planar rotations occur when the orientation of the target's rotation vector changes during the CPI relative to the radar.
2.  Large total changes in relative aspect angle. The ISAR signal processing chain assumes that a scatterer is contained within a range-bin during the CPI. When the target's change in relative aspect angle is large enough, scatterers will start to move across range-bins during the CPI. If the inverse Fourier transform is applied in this scenario, the final image will be blurred across the range-bins.

The RMC portion of the ISAR signal processing chain is structured into three distinct sections to minimise these effects without requiring any more information than that present in the range-Doppler image:

1.  An optimal time-window algorithm is applied to minimise the effect of both types of rotational blurring.
2.  A rotational velocity estimation algorithm is applied to scale the range-Doppler image.
3.  The rotational velocity is fed into a Polar Format Algorithm (PFA) to further reduce rotational blurring and increase cross-range resolution.

### 4.1 Optimal time-window algorithm

A subset of the range-profiles in a CPI can be used to form a rotationally de-blurred image of the target. The subset can be selected using a rectangular window with a given position and width. An image quality metric such as image contrast can be used to find the location and width of the rectangular window that gives the optimum image quality. Reference [9] discusses a two-step optimisation process for finding a suitable time-window. While this approach rotationally de-blurs the image, it also decreases the Doppler/cross-range resolution. The results are displayed below.
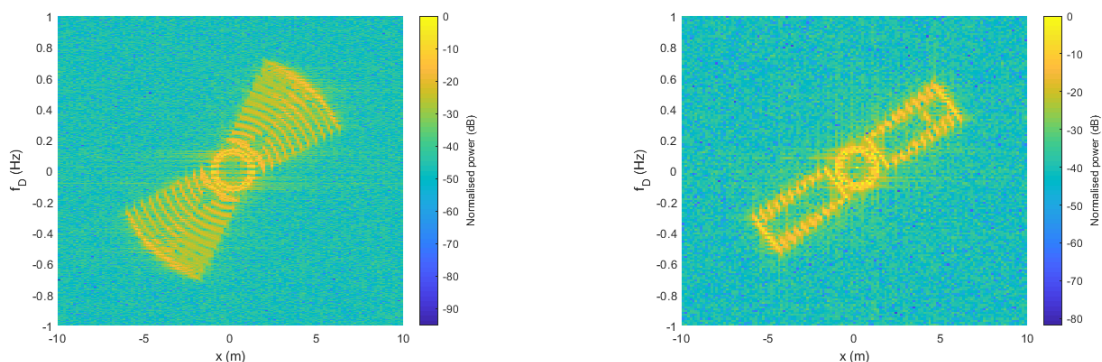


Fig. 6 Rotationally-blurred range-Doppler image before (left) and after (right) applying the Optimal Time-Window algorithm.

## 4.2    Rotational velocity estimation algorithm
Two distinct types of rotational velocity estimation algorithms will be discussed in this paper: chirp-rate estimation, and rotational correlation.

### 4.2.1    Chirp-rate estimation
The chirp-rate algorithms use the signal's phase information to estimate the rotational velocity. In equation 2, we approximated the trigonometric terms in the range equation for a scatterer to a first-order Taylor series expansion (up to linear terms). By approximating them using a second-order Taylor series expansion instead (up to quadratic terms), we can see that the rotation of the target results in a small chirp-rate, $m = \frac{2f_c}{c}x\dot{\varphi}^2$ in the phase of the range-profiles:

$$R_n \approx R_0 + x_n\left(1 - \frac{\varphi^2}{2}\right) - y_n\varphi$$

$$S_{corr}(x,\eta) \approx \sum_{n=1}^{N} B \cdot e^{j4\pi\frac{f_c}{c}\left[\left(x_n - y_n\dot{\varphi}\eta - \frac{1}{2}x_n\dot{\varphi}^2\eta^2\right) - x\right]} \cdot \text{sinc}\left\{\pi\frac{2B}{c}(x_n - x)\right\}$$

There are several methods to estimate the chirp-rate of a signal. In this paper we will compare the performances of the following algorithms for estimating the rotation rate of a target: Local Polynomial Fourier Transform (LPFT) [10], and Cubic Phase Function (CPF) [11]. In order to apply these methods, a range-bin containing a scatterer needs to be identified from the range-Doppler image. A Laplacian of Gaussian (LoG) blob detection algorithm can be used to do this [12]. The range-bin of the brightest scatterer within each blob is used.
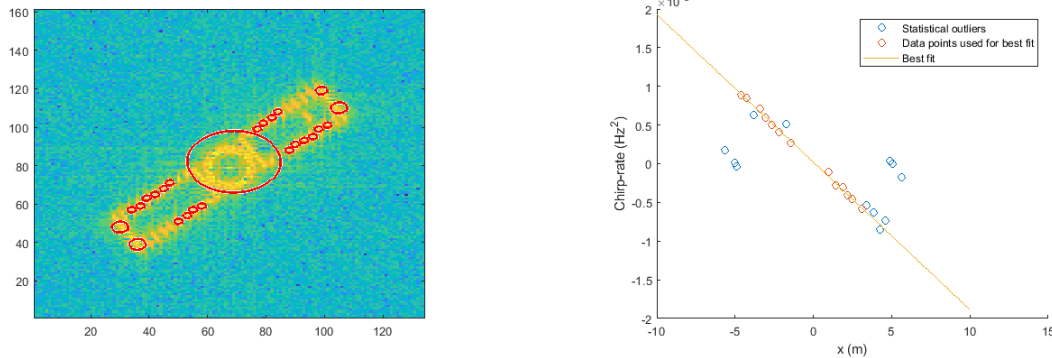


Fig. 7 LoG blob detection (left). Plot of chirp-rate against range for each blob (right).

Once identified, an inverse Fourier transform is applied to the chosen range-bin to convert it to a function of slow-time. The chirp-rate of this signal can now be evaluated. In order to obtain a good estimate of the rotation-rate, the chirp rate is measured for several other range-bins containing scatterers and the results are plotted. Since the chirp-rate is linearly dependent on the scatterer's position on the $x$-axis, the gradient of a line of best fit through the results ($\mu$) can be used to estimate the rotation rate, $|\dot{\varphi}| \approx \sqrt{c|\mu|/(2f_c)}$. The accuracy of the rotation rate estimate is improved by iteratively removing outliers from the plot before finding the line of best fit:

1.    A line of best fit is plotted through the data.
2.    The gradient of the line of best fit is used to estimate the rotation rate.
3.    Outliers are identified using Cook's distance.
4.    If there are no outliers, stop. Otherwise, remove the outliers from the dataset and return to step 1.

### 4.2.2    Rotational correlation
Alternatively, if two range-Doppler images are extracted from the CPI, the differences in their rotational position and the time difference between each image can be used to estimate the target's rotation rate. Reference [13] describes a method for estimating rotational velocity using correlation techniques. Joint Time Frequency Transform (JTFT) algorithms can be used to extract the two range-Doppler images required for rotational correlation. In this

paper we compare the performances of the following JTFT algorithms as inputs for the rotational correlation algorithm: Short Time Fourier Transform (STFT) [14], and Smoothed Pseudo Wigner-Ville Distribution (SPWVD) [15] [16].
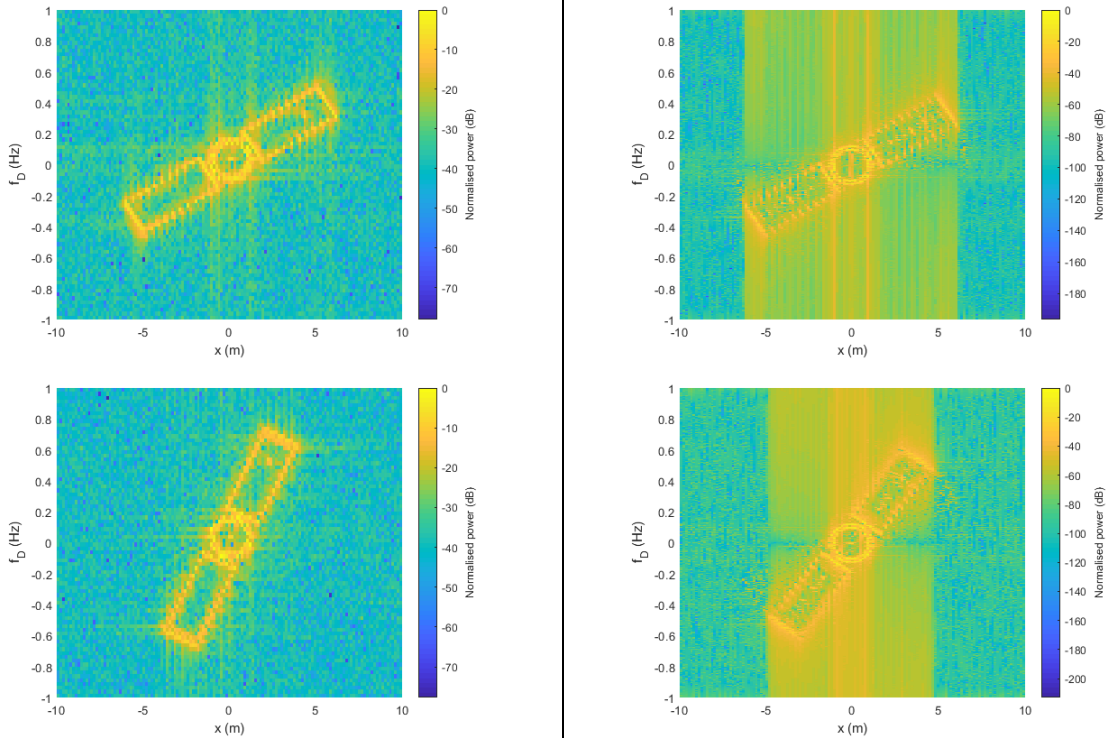


Fig. 8 Extracting range-Doppler images at two different time instances (top/bottom) by applying JTFT algorithms: STFT (left), SPWVD (right).

### 4.3    Polar Format Algorithm

We have previously used small angle approximations to form an image of the target; however we know that if this condition is not satisfied, the image will be rotationally-blurred. In the case where the small angle approximation doesn't hold, we may use equation 1 to describe the stretched-processed signals after TMC as:

$$s_{corr}(\Delta, \eta) \approx \sum_{n=1}^{N} e^{j2\pi[k_x x_n - k_y y_n]}$$

$$k_x = \left(f_0 + \frac{B}{\tau}\Delta\right)\cos[\varphi(\eta)] \quad \text{and} \quad k_y = \left(f_0 + \frac{B}{\tau}\Delta\right)\sin[\varphi(\eta)]$$

If we know the target's aspect angle at each slow-time sample (e.g. from the estimated rotational velocity, $\varphi(\eta) \approx \dot{\varphi}\eta$), we can polar format this data by interpolating it over an evenly spaced $(k_x, k_y)$ grid. Since the polar formatted data now follows the rotation of the target, scatterers do not move across data bins enabling a direct Fourier transform without blurring. Since the total change in aspect angle can now be bigger without causing blurring, the cross-range resolution of the image will be improved, $\Delta y = \frac{c}{2f_c \dot{\varphi} CPI}$. Three interpolation algorithms are discussed in this paper: bilinear [17], 1st Order Nearest Neighbour (NN1) [18], 2nd Order Nearest Neighbour (NN2) [18].

### 4.3.1    Target centring

PFA can only be applied successfully when the target's centre of mass/rotation is located at (0, 0) in the range-Doppler image. An algorithm has been developed to account for any misalignment that may occur after TMC:

1.    Range and Doppler offsets are specified: $\delta x, \delta f_D$.

2. An inverse Fourier transform is applied to the range profiles after TMC to get a matrix of corrected de-chirped signals.
3. The location of the target in the image is shifted by multiplying the corrected de-chirped signals by the following function:

$$m(\Delta, \eta) = e^{-j\frac{4\pi}{c}\left[f_0 + \frac{B}{\tau}\Delta\right]\delta x} \cdot e^{j2\pi\eta\delta f_D}$$

4. PFA is then applied using the estimated rotational velocity and the image contrast is evaluated.

Since the image will be blurred when the target is poorly centred, optimum range and Doppler offsets can be found by maximising the image contrast using a Nelder-Mead approach. The centre of mass of the range-Doppler image can be used as an initial guess for the range and Doppler offsets.

### 4.3.2 Optimal Time-Window with PFA

If the target's rotation is planar and its centre of rotation and rotational velocity are known perfectly, then PFA can be applied to the entire CPI. This results in a de-blurred image with maximum cross-range resolution. Unfortunately, it's uncommon that all these conditions are satisfied; however by applying the optimal time-window algorithm in combination with images produced using PFA, a larger time-window can be found that improves the cross-range resolution of the final image without adding excessive blurring.

## 5. MOTION COMPENSATION ALGORITHM SELECTION

### 5.1 TMC algorithm selection

A combination of TMC algorithms such as those specified in Section 3 have been used to form the TMC portion of the ISAR signal processing chain. We will not cover the selection of these algorithms in any more detail in this paper.

### 5.2 RMC algorithm selection

In order to select suitable RMC algorithms for space object imaging, their performances were evaluated against a representative scenario – a point scatterer target rotating with a constant rotational velocity. The 2D point scatterer target shown in Fig. 1 was used for the tests. The following radar parameters were used in the tests:

| | |
|---|---|
| Centre frequency ($f_c$) | 100 GHz |
| Bandwidth ($B$) | 10 GHz |
| Pulse Repetition Frequency ($PRF$) | 200 Hz |
| Pulse width ($\tau$) | 100 μs |
| Coherent Processing Interval ($CPI$) | 100 s |

Table 1 – Parameters used to test the performance of the RMC algorithms

The optimal time-window algorithm was the only method considered in this paper to reduce the effect of non-planar rotations. It was therefore decided that it should be included in the ISAR signal processing chain. Since the output of the optimal time-window algorithm will impact the performance of the other RMC algorithms, it was included in the following tests.

In contrast, since we aren't considering TMC algorithm selection in this paper, perfect TMC was applied to the stretch-processed signals using known translational motion parameters from the simulation.

**Rotational velocity estimation algorithm analysis:**
The performance of the two chirp-rate estimation algorithms (LPFT, CPF) and the two rotational correlation algorithms (STFT, SPWVD) against a selection of representative rotational velocities is plotted below. Performance of the algorithms was determined by adding noise to the range profiles resulting in a constant 15 dB SNR. Each data-point in the plots represents the mean of five tests. The results in Fig. 9 show that the chirp-rate algorithms (LPFT, CPF) are better suited to estimating rotational velocities after optimal time windowing than the rotational correlation algorithms (STFT, SPWVD). This is likely because the rotational correlation algorithms require the scatterers to move between pixels in the two images; however, the optimal time-window algorithm restricts the CPI to reduce blurring by keeping the scatterers within one pixel.

Of the chirp-rate algorithms, the CPF chirp-rate estimation algorithm appears to have lower relative error than the LPFT chirp-rate estimation algorithm in almost all occasions apart from four instances when $\dot{\varphi} \approx 1\,°/s$, where it exceeds 100 %. In contrast, the relative error due to the LPFT chirp-rate estimation algorithm is more consistent and is contained entirely between 0.1 – 40 %.
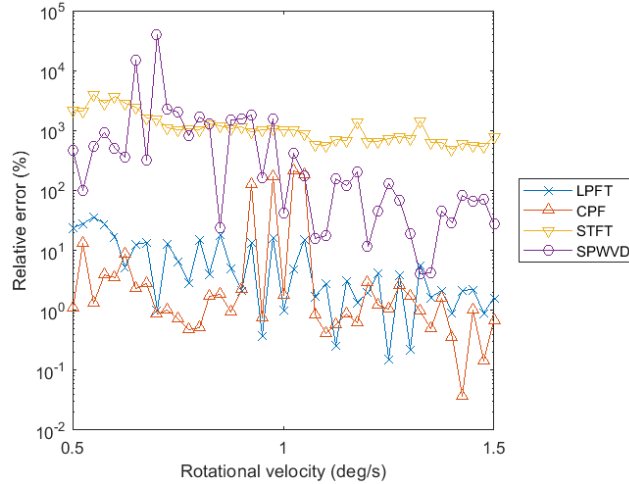


Fig. 9 Error between true rotational velocity and estimated rotational velocity for $SNR = 15\,dB$.

Further analysis showed that a line of best fit produced from the chirp-rate measurements with a smaller Root Mean Square Error (RMSE) generally resulted in a better estimate of the target's true rotational velocity. It was therefore decided that the signal processing chain should incorporate both chirp-rate measurement techniques. The RMSE of the fit resulting from each approach could then be measured and used to decide which rotational velocity estimate to use. This gives the advantage of being able to use the more accurate CPF algorithm for most cases while the LPFT algorithm is able to catch any outliers. The LPFT algorithm is significantly faster than the CPF algorithm. This means that the computational burden of adding this extra step is relatively small.
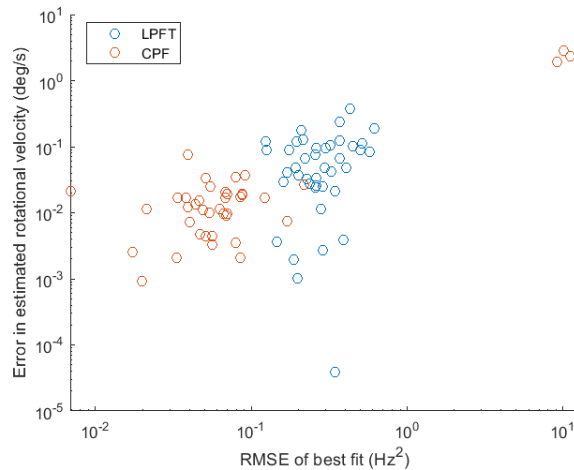


Fig. 10 A graph showing that a lower RMSE of best fit generally results in a more accurate estimate of the target's true rotational velocity.

**PFA interpolation algorithm analysis:**
The performance of the three PFA interpolation algorithms (Bilinear, NN1, NN2) against a selection of representative rotational velocities is plotted below. Like in the previous set of tests, performance of the algorithms against rotational velocity was determined by adding noise to the range profiles resulting in a constant 15 dB SNR. Like before, each data-point in the plots represents the mean of five tests. The percentage increase in image contrast resulting from the implementation of the PFA algorithms is measured relative to the optimal time-windowed range-

Doppler image for the same input parameters. The target's centre of rotation has been positioned at (0, 0) to avoid the impact of the target centring algorithm (Section 4) on the results. We have also applied PFA using the precise rotational velocity of the target to avoid the impact of the rotational velocity estimation algorithms (Section 4).
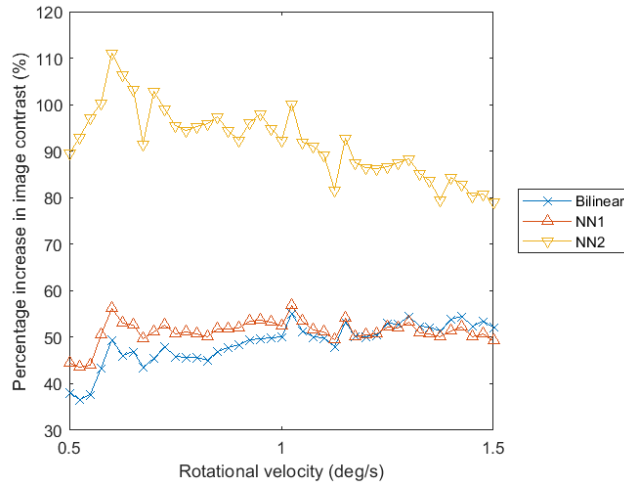


Fig. 11 Percentage increase in image contrast relative to the optimal time-windowed range-Doppler plot for SNR = 15 dB.

The results in Fig. 11 show that the 2nd Order Nearest Neighbour (NN2) interpolation algorithm produces the best improvement in image quality for all rotational velocities of interest. Because perfect inputs have been given for PFA (exact rotational velocity, perfect centring), we expect the percentage improvement in image contrast to be lower in practice.

### 5.3 Proposed ISAR signal processing chain
The conclusions of the previous section have resulted in the selection of the RMC algorithms. The proposed end-to-end ISAR signal processing chain is displayed in the diagram below.
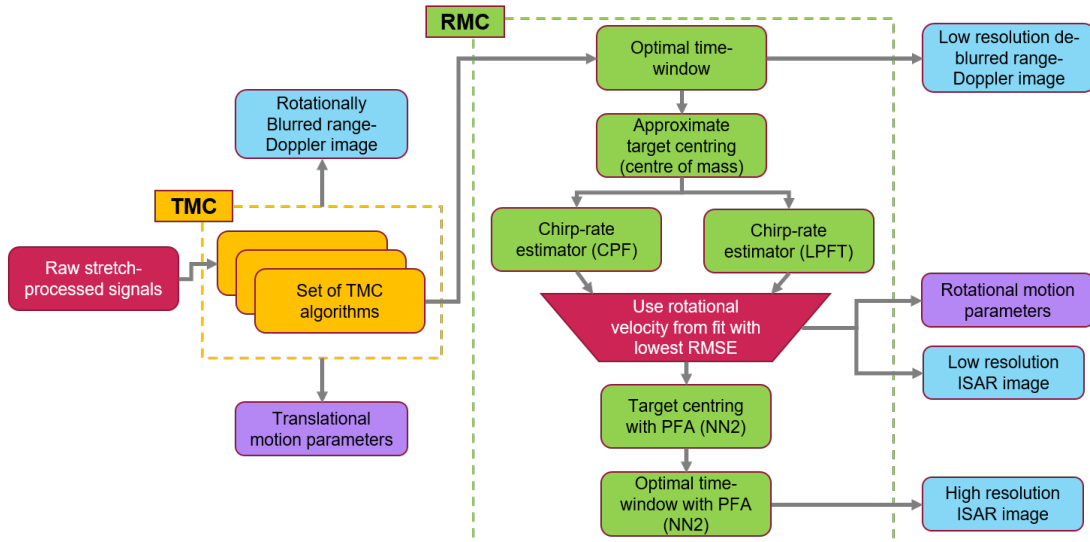


Fig. 12 Proposed ISAR signal processing chain with details of chosen algorithms and tap off points.

## 6. APPLICATION AGAINST REPRESENTATIVE ORBITAL SCENARIOS

The proposed end-to-end ISAR signal processing chain is now ready to be tested against a set of representative orbital scenarios. The purpose of these tests is to determine the impact of an orbital target's relative on the quality of

the ISAR image produced by the proposed signal processing chain. For this reason, amplitude variations due to the radar range equation have been ignored and all images have been normalised.

## 6.1    Simulation geometry

For an orbital scenario, the rotational motion of a target perceived by a radar results from the combination of the satellite's orbital motion, the Earth's rotation and the target's attitude mode. We will briefly discuss the assumptions and methodology chosen to model each of these factors here:

**Orbital propagation:**

It was assumed that the effect of orbital perturbations on the trajectory of a target during a single pass will likely be minimal. We therefore chose to use a basic two-body propagator as it allowed us to use inputs that resulted in precise and repeatable trajectories. The orbital propagator was used to determine the location of the target's centre of mass relative to an Earth Centred Inertial (ECI) reference frame for each pulse in the radar's CPI. The target motion was modelled as a circular orbit as this is the most common orbit type in LEO.

**Radar geometry:**

A simple oblate spheroid model of Earth was used to model the position of the radar. This allowed us to approximately define the latitude/longitude/altitude of the radar and determine its location relative to the ECI frame. The radar's position relative to the ECI frame was updated for each pulse in the radar's CPI as Earth rotated.

**Target attitude:**

Two attitude modes were simulated: nadir-pointing, and tumbling. Quaternions were used to rotate the spacecraft to model these attitude types. For the nadir-pointing case, the z-axis of the satellite's body-fixed frame was aligned to point towards Earth's centre of mass while the x-axis of the satellite's body fixed frame was aligned parallel to the spacecraft's velocity vector. For the tumbling case, the target rotated about its y-axis at a constant rate. In the tumbling case, the y-axis was fixed relative to the ECI frame.

## 6.2    Point scatterer model

A 3D point scatterer model based on a generic "box with wings" was used and is shown in Fig. 13 (left). A Hidden Point Removal (HPR) algorithm was implemented to better portray how a real ISAR image may look. The method is outlined in [19]. Note that the goal of this work isn't to accurately simulate ISAR returns, but to evaluate the performance of the signal processing chain. This feature was added to see if occlusion impacted the proposed signal processing chain.
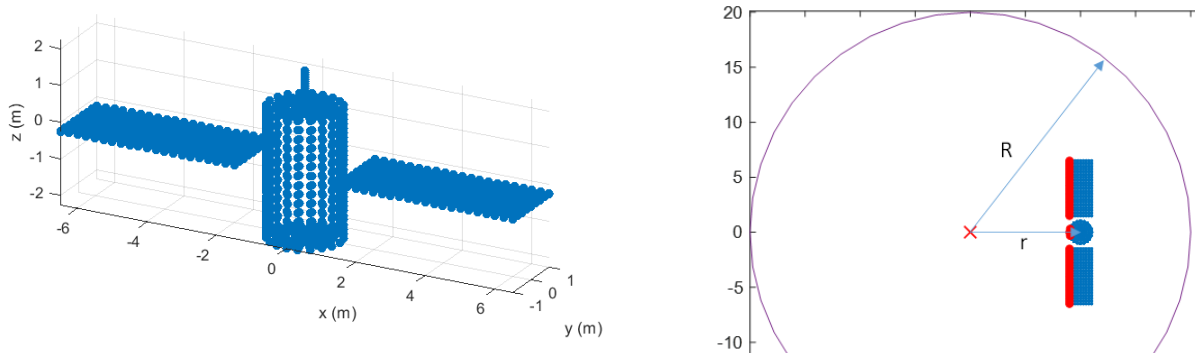


Fig. 13 (Left) Generic "box with wings" point scatterer model. (Right) Example of HPR – the observer is at (0,0), the target scatterers are shown in blue, the inverted scatterers are shown in green, and the scatterers on the convex hull are shown in red. Note that the values of r, R are smaller than usual for diagrammatic purposes.

The HPR method involves two steps: inversion (1) and convex hull construction (2). Inversion is carried out by mirroring the target scatterer points across the surface of a sphere of radius R. The inverted scatterers can then be used to find the observable surface of the target. This is done by generating a convex hull over the inverted scatterers. The scatterers that do not define the convex hull of the inverted surface are assumed not to be visible to the observer. Fig. 13 (right) shows an example of HPR in 2D. Smaller values of R result in fewer points defining the convex hull. Therefore as R increases, more points become visible. For the representative orbital scenarios, a value of R was chosen so that roughly half the scatterers could be seen for most orientations. These threshold values are

sensitive to target scatterer density so new values of R must be chosen for each target. While this methodology doesn't accurately generate the received signal from a target, it gives a better representation of the final ISAR image.

### 6.3 Simulation parameters

The following scenario parameters were used in the tests:

| | |
|---|---|
| Radar latitude | 50 ° |
| Radar longitude | 0 ° |
| Radar altitude | 0 m |
| Target's maximum orbital elevation relative to the radar's horizon | 60 ° |
| Target's azimuth at maximum orbital elevation relative to the radar's horizon | 0 ° |
| Target altitude | 500 km |
| Minimum elevation that the radar can observe the target | 25 ° |
| Time at target's peak elevation relative to radar's horizon | 12:00:00 20th July 2023 |
| Target tumble rate about body-fixed y-axis (*valid for tumbling scenarios) | 0.15 °/s |

Table 2 – Scenario parameters used to test the performance of the proposed ISAR signal processing chain.

Note that since this paper is only looking at the impact of the choice of signal processing algorithms on the final image, hardware and physical constraints (such as eclipsing) have been ignored. The following radar parameters were used in the tests:

| | |
|---|---|
| Centre frequency ($f_c$) | 100 GHz |
| Bandwidth ($B$) | 10 GHz |
| Pulse Repetition Frequency ($PRF$) | 200 Hz |
| Pulse width ($\tau$) | 100 µs |
| Coherent Processing Interval ($CPI$) | 100 s |
| Sampling frequency ($f_{samp}$) | 13.3 MHz (unambiguous range extent of 20 m) |
| Average range profile SNR | 15 dB |

Table 3 - Parameters used to test the performance of the proposed ISAR signal processing chain.
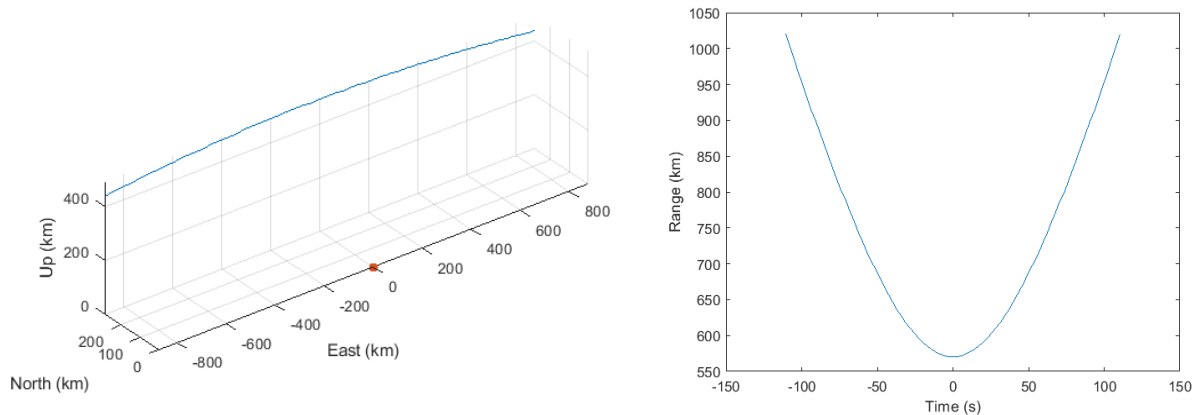


Fig. 14 (Left) Trajectory of the target's centre of mass relative to the radar. (Right) Distance between the radar and the target's centre of mass as a function of time.

### 6.4 TMC

This paper will not evaluate the performance or impact of the choice of TMC algorithms on the quality of the resulting image. We have therefore applied perfect TMC to the range profiles (with a small range offset to test the target centring algorithm). The range-Doppler images resulting from the aforementioned parameters after perfect TMC are shown below – note that the simulations were run so that the centre of the CPI was aligned with when the target reached its maximum elevation relative to the radar's horizon.
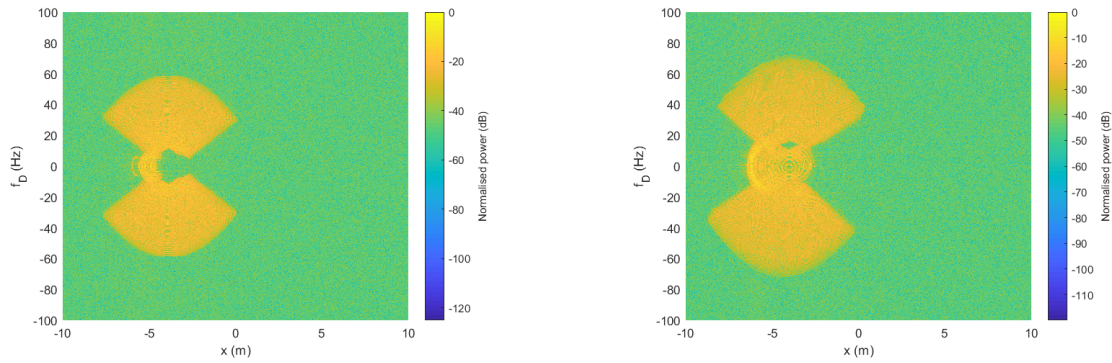
Fig. 15 Rotationally blurred range-Doppler image of nadir-pointing target (left) and tumbling target (right).

## 6.5 Optimal time-window

**T**he optimal time-window algorithm requires an initial estimate of the window width to determine the optimal position of the window. It then fixes that location and finds the optimal window width. However since the data stored during the CPI is finite, the window width cannot extend beyond $\eta = 0$ or $\eta = CPI$. Therefore, although using a small initial estimate of the window width gives greater positional freedom, if the optimal location is found near $\eta = 0$ or $\eta = CPI$, the ability to increase the window width is limited. We found that using an initial estimate of 20% of the CPI was an effective tradeoff between these factors.
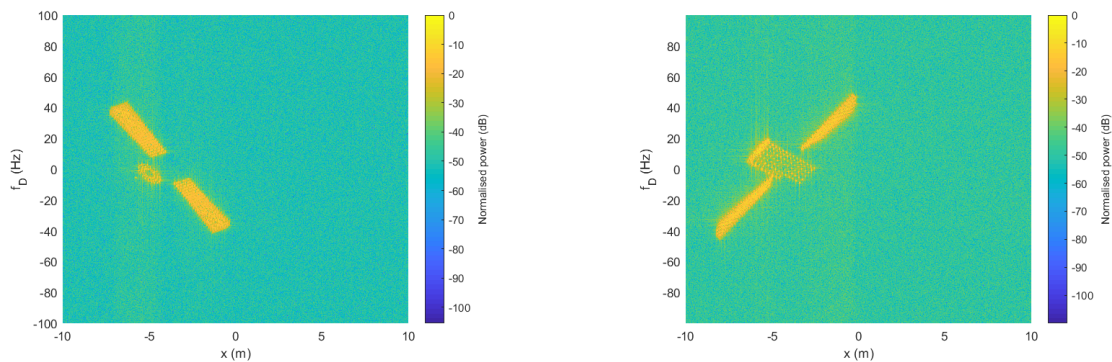


Fig. 16 Low-resolution, rotationally de-blurred range-Doppler image of nadir-pointing target (left) and tumbling target (right) after applying the optimal time-window algorithm to the results shown in Fig. 15.

## 6.6 Rotation-rate estimation

The first step in the LoG blob detection algorithm is to normalise the image to be analysed. If the maximum pixel value within a blob is less than the specified threshold, the blob is removed. Since the threshold is always compared against a normalised scale, its effect is consistent across all images. We found that a threshold of 0.1 worked well in the RMC algorithm analysis in section 5. We therefore decided to use the same threshold here.
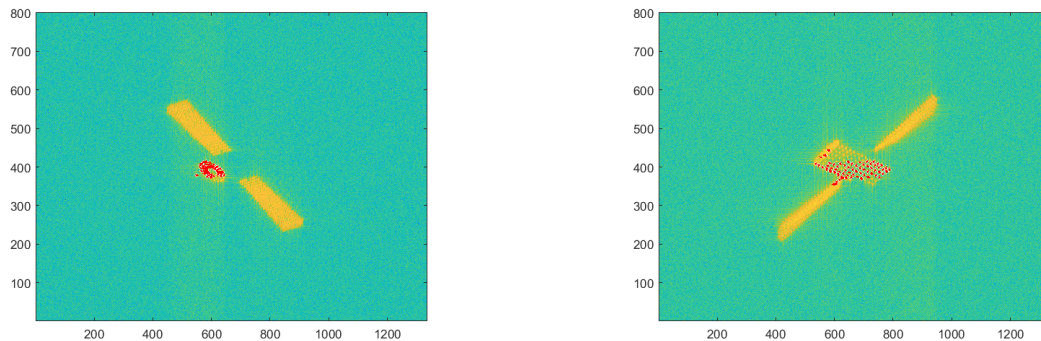


Fig. 17 Result of applying the LoG blob detection algorithm on the range-Doppler images of the nadir-pointing target (left) and tumbling target (right) – blobs shown in red.

The detected blobs were then used to estimate the rotational velocity of the target using the LPFT and CPF chirp-rate estimation techniques. Both fits for the tumbling target had lower RMSE than those for the nadir-pointing target. This is likely due to a greater spread in blobs along the $x$-axis for the tumbling target. Only a small percentage of the chirp-rate estimates were excluded from the best fit calculations for either scenario. In both cases, the CPF algorithm resulted in a lower RMSE.
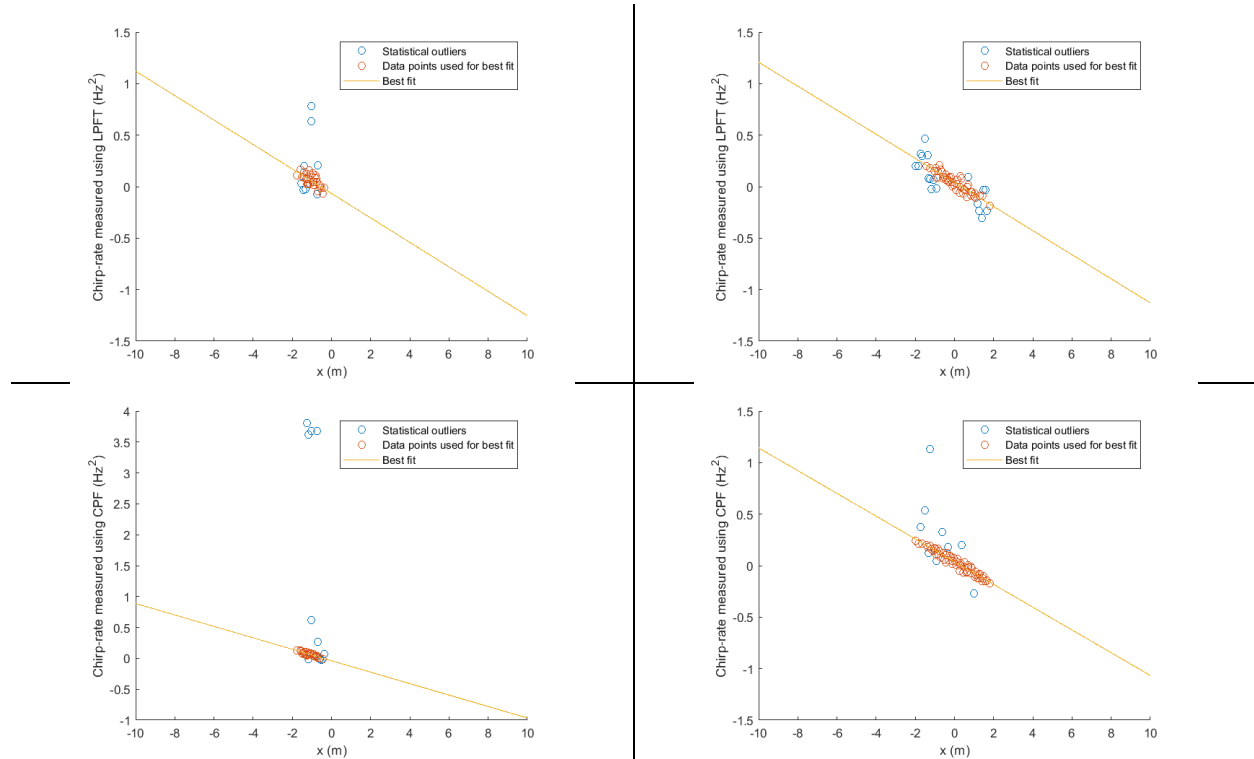


Fig. 18 Plot of chip-rate against range using data points from the LoG blob detection algorithm: nadir-pointing target using LPFT (top left) and CPF (bottom left), tumbling target using LPFT (top right) and CPF (bottom right).

The rotational velocities estimated from the line of best fit enabled us to scale the range-Doppler axes appropriately. Comparing the scaled images against the true dimensions of the 3D point scatterer model, the estimated rotational velocities appear to be approximately correct.
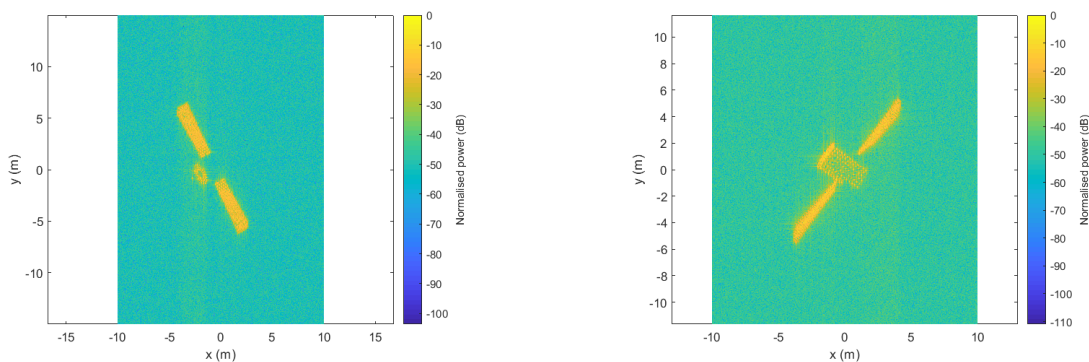


Fig. 19 Low resolution ISAR images are formed after estimating the target's rotational velocity by scaling the Doppler axis appropriately: nadir-pointing target (left), tumbling target (right).

## 6.7    Optimal time-windowed PFA

Applying the optimal time-windowed PFA algorithm further improves the quality of the final image, particularly in the regions furthest from the centre of rotation such as at the tips of the "wings". This will improve the ability to do

further image analysis if required. Note that the orientation of the targets are slightly different after applying this algorithm. This is because PFA uses angles calculated by multiplying the estimated rotational velocity with times from the time window. Since the times in the time window don't start at zero, the angles used for PFA also don't start at zero. The result is an image matching the orientation expected at the centre of the CPI.
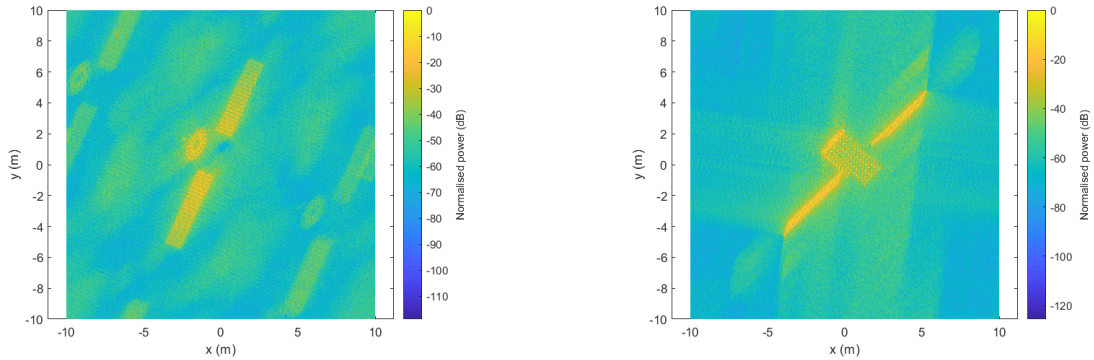


Fig. 20 High resolution ISAR images formed by applying optimal time-windowed PFA using the estimated rotational velocity: nadir-pointing target (left), tumbling target (right).

The resulting images display some aliasing due to imperfect rotational velocity estimation and imperfect target centring, however the amplitude of the aliasing is relatively low. Image analysis techniques can extract useful information from these images while ignoring aliased components. For example, a simple threshold of -30dB has been applied in Fig. 21 to pick out the scatterers more clearly. More advanced image analysis techniques can be used to suppress sidelobes (e.g. window functions [20]) and to extract scatterer locations (e.g. CLEAN [2]).
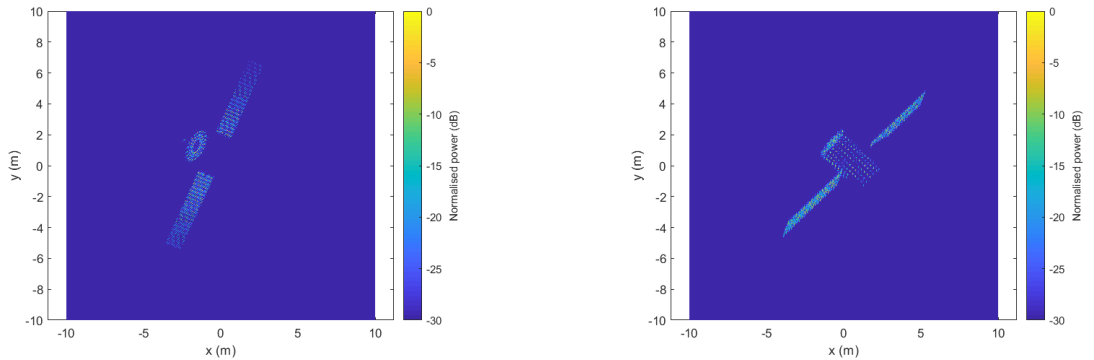


Fig. 21 Result of thresholding ISAR images formed using PFA: nadir-pointing target (left), tumbling target (right).

## 7. APPLICATION AGAINST AN RPO SCENARIO

### 7.1 Clohessey-Wiltshire equations

The Clohessey-Wiltshire (CW) equations describe a first-order approximation of the relative motion between a target in a circular orbit and a chaser spacecraft in an elliptical orbit. The Local Vertical Local Horizontal (LVLH) frame is used to describe the CW equations. If the position and specific angular momentum vectors of the target in an Earth Centred Inertial (ECI) frame are given by $\vec{r}, \vec{h}$ then: the $x$-axis of the LVLH frame is parallel to the $\vec{r}$ vector (R-bar); the $z$-axis of the LVLH frame is parallel to the $\vec{h}$ vector; the $y$-axis of the LVLH frame makes up the right-hand rule (V-bar). This means that the LVLH frame rotates relative to the inertial frame as the target moves along its orbit. The CW equations are given by a set of differential equations. These equations have a closed-form solution given by:

$$x = [4 - 3\cos(nt)]x_0 + \left[\frac{\sin(nt)}{n}\right]\dot{x}_0 + \frac{2}{n}[1 - \cos(nt)]\dot{y}_0$$

$$y = 6[\sin(nt) - nt]x_0 + y_0 + \frac{2}{n}[\cos(nt) - 1]\dot{x}_0 + \frac{1}{n}[4\sin(nt) - 3nt]\dot{y}_0$$

$$z = \cos(nt)\, z_0 + \frac{1}{n}\sin(nt)\, \dot{z}_0$$

Where $n = \sqrt{\mu/a^3}$ is the orbital rate of the target body, $a$ is the semi-major axis of the target orbit and $\mu$ is the standard gravitational parameter of Earth. If the initial velocity of the chaser spacecraft relative to the target is given by $\dot{x}_0 = -2nx_0$ and $\dot{y}_0 = \frac{n}{2}y_0$, then the closed-form solution now describes an ellipse with a semi-minor axis of $C = \sqrt{x_0^2 + (y_0^2/4)}$ and an initial starting angle of $\theta^* = \tan^{-1}(2x_0/y_0)$ in the $x, y$ plane. Non-zero values of $z_0, \dot{z}_0$ result in oscillations perpendicular to the $x, y$ plane, but do not disturb the elliptical motion. Since this relative motion results from the natural motion of the two orbits, in this paper we have called it a Natural Circumnavigation Ellipse (NCE).

## 7.2 RPO scenario

The NCE was used as a scenario to test the proposed ISAR signal processing chain. The NCE exhibited the following parameters:

| | |
|---|---|
| NCE semi-minor axis ($C$) | 1 km |
| Chaser spacecraft angle measured clockwise from V-bar at the centre of the CPI ($\theta^*$) | 30 ° |
| Out of plane oscillation amplitude ($z_{max}$) | 0.2 km |
| Location of maximum out of plane oscillation as an angle measured clockwise from V-bar ($\theta^*_{z\,max}$) | 90 ° |

Table 4 – Scenario parameters used to define the trajectory of the chaser spacecraft.

The target and radar parameters are identical to those used in section 6. The target spacecraft was simulated to be nadir-pointing while the chaser spacecraft was simulated to point towards the target spacecraft during the RPO.
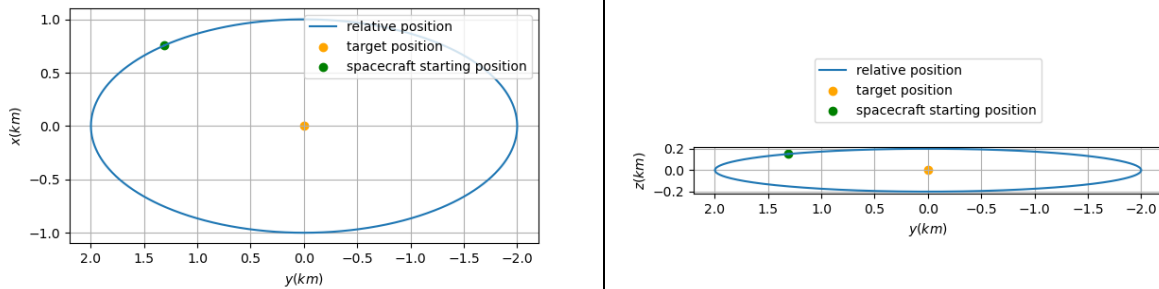


Fig. 22 Trajectory of the chaser spacecraft relative to the target spacecraft in the Clohessey-Wiltshire frame projected onto the x,y (left) and y,z (right) planes.

## 7.3 Scenario analysis

Imaging this scenario using ISAR can be achieved in a number of ways. For example, if the two spacecraft can be detected simultaneously (i.e. similar range and close in angle), then the sample rate, $f_{samp}$ can be adjusted to form an unambiguous range extent that encompasses both objects. In order to form a clear image, TMC needs to be applied to both sets of range profiles individually. This means that the two range profiles need to be separated. Separation is very difficult when the range profiles cross over, but an image could be formed by using a subset of range profiles before or after this event.

Fig. 23 shows the range-Doppler image formed by this method. A separation distance of 30 m has been specified so that the satellites are not co-centred at $x = 0$. After TMC the only Doppler information present from both satellites is from their independent rotations. The images of both satellites are therefore centred at $f_D = 0$ and lack any cross-range displacement information. Furthermore, since the satellites are rotating at different rates, two different scaling factors are required to convert the Doppler axis to a cross-range axis. Each image therefore needs to be scaled separately. Finally, since the estimated range/velocity of the target spacecraft is used to de-chirp the LFM pulses, the image of the chaser spacecraft exhibits some smearing due to poor de-chirping.
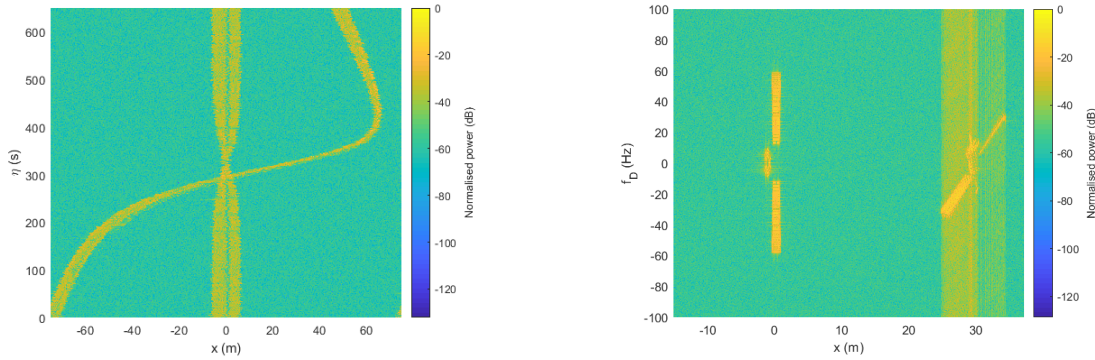
Fig. 23 (Left) Range profiles resulting from an RPO scenario where both spacecraft are detected at once using stretch processing. (Right) Range-Doppler image resulting from applying TMC to the range profiles on the left – note that the range extent has been trimmed.

For the reasons specified above, it is usually easier to image the spacecraft separately in almost all situations. The signal processing chain proposed in this paper can then be used to de-blur and scale the two images individually. If the CPIs are kept short and the images are captured in quick succession, the orientation of the two spacecraft in the images will approximately match the orientation expected if the images were captured simultaneously.
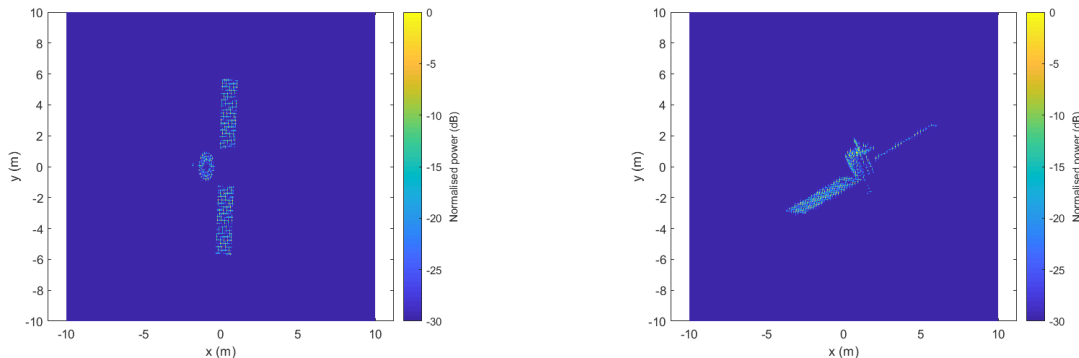


Fig. 24 ISAR image of nadir-pointing target satellite (left) and RPO-tracking chaser satellite (right) after applying proposed ISAR signal processing chain and manual thresholding.

If desired, the images can be overlaid using positional information derived from the assisting tracker system. The range displacement required between the images is already known from the range measurements. The cross-range displacement can be inferred from the orbital trajectory. Fig. 25 (left) demonstrates how this may look.
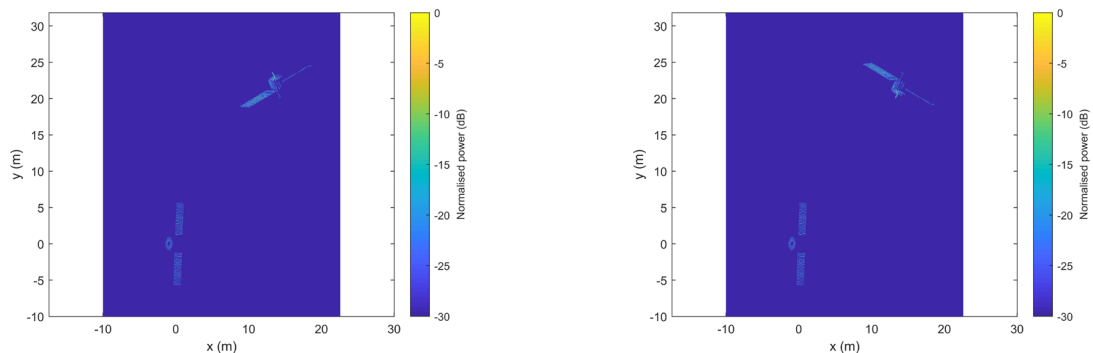


Fig. 25 (Left) Image of an RPO scenario constructed from ISAR images of the two targets and knowledge of their relative positions – note that the spacing between the two satellites has been significantly reduced for diagrammatic reasons. (Right) The same image of the RPO scenario corrected for the chaser spacecraft's negative rotational velocity.

Notice that the chaser satellite in the top right of the image isn't pointing towards the target satellite when we expect it to. This is because the chirp-rate algorithms give the magnitude of the estimated rotational velocity, but cannot determine whether it is positive or negative. In contrast, the rotational correlation algorithms do identify the direction of the rotational velocity. The positive/negative information from a rotational correlation algorithm can be used to augment the final image. Doing this results in Fig. 25 (right) showing the chaser spacecraft pointing towards the target spacecraft.

## 8.   CONCLUSIONS

In this paper we have designed and tested a proposed signal processing chain for LEO ISAR SOI against a set of representative scenarios. The proposed signal processing chain demonstrated good de-blurring and scaling of the ISAR image for both scenarios. We further tested the performance of the signal processing chain for producing resolved images of RSOs undergoing close-proximity manoeuvres. We concluded that maximum benefit is attained when the ISAR images of an RPO scenario are augmented with additional positional information attained by a tracking radar.

## 9.   REFERENCES

[1]   ESA, "Space Environment Statistics," [Online]. Available: https://sdup.esoc.esa.int/discosweb/statistics/. [Accessed 21 August 2023].

[2]   Choi et al, "Two-Dimensional Evolutionary Programming-Based CLEAN," IEEE, 2002.

[3]   Eshbaugh et al, "HUSIR Signal Processing," Lincoln Laboratory Journal, 2014.

[4]   Chen et al, "Target-Motion-Induced Radar Imaging," IEEE, 1979.

[5]   Itoh et al, "Motion Compensation for ISAR Via Centroid Tracking," IEEE, 1996.

[6]   Xi et al, "Autofocusing of ISAR Images Based on Entropy Minimization," IEEE, 1999.

[7]   Martorella et al, "Contrast Maximisation Based Technique for 2-D ISAR Autofocusing," IET, 2005.

[8]   Wahl et al, "Phase Gradient Autofocus - A Robust Tool for High Resolution SAR Phase Correction," IEEE, 1994.

[9]   V. C. Chen and M. Martorella, Inverse Synthetic Aperture Radar Imaging, SciTech Publishing, 2014.

[10] Martorella, "Novel Approach for ISAR Image Cross-Range Scaling," IEEE, 2008.

[11] Du et al, "An Accurate Two-Step ISAR Cross-Range Scaling Method for Earth-Orbit Target," IEEE, 2017.

[12] Lindeberg, "Feature Detection with Automatic Scale Selection," KTH (Royal Institute of Technology), Stockholm, Sweden, 1998.

[13] Park et al, "Cross-Range Scaling Algorithm for ISAR Images Using 2-D Fourier Transform and Polar Mapping," IEEE, 2011.

[14] S. Qian and D. Chen, Joint Time-Frequency Analysis Methods and Applications, Prentice Hall PTR, 1996.

[15] Claasen et al, "The Wigner Distribution - A Tool for Time-Frequency Signal Analysis," Philips Journal of Research, 1980.

[16] Pikula et al, "A New Method for Interference Reduction in the Smoothed Pseudo Wigner-Ville Distribution," Brno University of Technology, 2020.

[17] M. Abramowitz and A. I. Stegun, Handbook of Mathematical Functions, United States Department of Commerce, 1970.

[18] Mersereau et al, "Digital Reconstruction of Multidimensional Signals from Their Projections," IEEE, 1974.

[19] Katz et al, "Direct Visibility of Point Sets," ACM Transactions on Graphics, 2007.

[20] C. Özdemir, Inverse Synthetic Aperture Radar Imaging with MATLAB Algorithms, John Wiley & Sons, Inc., 2021.